

Probing hundreds of individual quantum defects in polycrystalline and amorphous alumina

Chih-Chiao Hung,^{1,2,3} Liuqi Yu,^{1,2} Neda Foroozani,^{1,2} Stefan Fritz,⁴ Dagmar Gerthsen,⁴ and Kevin D. Osborn^{1,2,5}

¹Laboratory for Physical Sciences, 8050 Greenmead Drive, College Park, Maryland 20740, USA

²Quantum Materials Center, University of Maryland, College Park, Maryland 20742, USA

³Department of Physics, University of Maryland, College Park, Maryland 20742, USA

⁴Laboratory for Electron Microscopy, Karlsruhe Institute of Technology, Karlsruhe, 76131, Germany

⁵Joint Quantum Institute, University of Maryland, College Park, MD 20742, USA

(Dated: June 18, 2022)

Quantum two-level systems (TLSs) are present in the materials of qubits and are considered defects because they limit qubit coherence. For superconducting qubits, the quintessential Josephson junction barrier is made of amorphous alumina, which hosts TLSs. However, TLSs are not understood generally – either structurally or in atomic composition. In this study, we greatly extend the quantitative data available on TLSs by reporting on the physical dipole moment in two alumina types: polycrystalline γ – Al_2O_3 and amorphous α – AlO_x . To obtain the dipole moments p_z , rather than the less-structural coupling parameter g , we tune individual TLSs with an external electric field to extract the p_z of the TLSs in a cavity QED system. We find a clear difference in the dipole moment distribution from the film types, indicating a difference in TLS structures. A large sample of approximately 400 individual TLSs are analyzed from the polycrystalline film type. Their dipoles along the growth direction p_z have a mean value of 2.6 ± 0.3 Debye (D) (0.54 ± 0.06 eÅ) and standard deviation $\sigma = 1.6 \pm 0.2$ D (0.33 ± 0.03 eÅ). The material distribution fits well to a single Gaussian function. Approximately 200 individual TLSs are analyzed from amorphous films. Both the mean $p_z = 4.6 \pm 0.5$ D (0.96 ± 0.1 eÅ) and $\sigma = 2.5 \pm 0.3$ D (0.52 ± 0.05 eÅ) are larger. Amorphous alumina also has some very large p_z , > 8.6 D (1.8 eÅ), in contrast to polycrystalline which has none of this moment. These large moments agree only with oxygen-based TLS models. Based on data and the candidate models (delocalized O and hydrogen-based TLSs), we find polycrystalline alumina has smaller ratio of O-based to H-based TLS than amorphous alumina.

INTRODUCTION

Long coherence times are essential for quantum information processing and this implies high-quality Josephson junctions (JJs) in superconducting qubits [1–6]. For over a dozen years, quantum tunneling two-level systems (TLSs) have been known to be defects that cause loss and limit coherence of qubits [7, 8]. In addition, TLSs create telegraphic noise and $1/f$ noise [9–11] in superconducting qubits [12–14], semiconducting qubits [15], and astronomy photon detectors [16, 17]. There are several strategies to improve the qubit coherence time such as material optimization [18–21], surface treatments [21–23], and engineering of the qubit geometry to decrease the participation of TLSs [24–26].

In the quintessential JJ, an amorphous alumina barrier is grown thermally on the surface of aluminum [1, 2, 4]. Loss tangents of amorphous alumina in JJs [18] and in grown films [27] are measured to be approximately 2×10^{-3} , much higher than that in crystalline alumina from the sapphire substrates used for qubit fabrication [28]. Accordingly, amorphous materials are believed to have higher loss than crystalline ones due to additional tunneling degrees of freedom (TLSs) in the former. HBN and other 2D materials are being investigated for JJs [29–31], but an alternative method to improve the JJ barrier uses annealed crystalline alumina [32, 33]. Crystalline alumina studies show a decrease in both TLS density

[32] and TLS-qubit couplings, g , relative to amorphous alumina [33].

Recent TLS analysis techniques use dc-tuned electric [34–37] or strain field [38–40] for the observation of individual nanoscale defects. According to the Standard Tunneling Model (STM) [41, 42], individual TLSs have a dipole moment p , transition energy E and tunneling energy Δ_0 . Generally, the TLS is described as tunneling charge presumed to be an atom or small group of atoms, though a recent study reports on a possibility of trapped quasiparticles [43]. Their identification is a 50 years old mystery [44].

TLSs have an ac-coupling to quantum systems,

$$g = \frac{\Delta_0}{E} \frac{2p_z E_{rms}}{\hbar}, \quad (1)$$

which is related to dipole moment component p_z along zero-point fluctuation of electric field \mathbf{E}_{rms} . However, the most common measurement of g does not allow extraction of p_z because Δ_0 is unknown or E_{rms} is not uniform [8, 32, 33]. On the other hand, static dc-tuned measurements allow measurements of individual p_z [34, 35] and dynamically biased experiments extract averaged p_z [45]. Such dynamical bias can induce Landau-Zener transitions, and recent work shows that a resonator can even exhibit dynamical decoupling using these transitions [46]. Recently, voltage bias gates are added above or below the target area to tune TLSs [36, 37]. The extractions of

dipoles are possible from g and extracted position, but the distribution is given as a function of g rather than p_z [36]. Also, only small samples of p_z were directly extracted in the past: 13 in amorphous alumina [35] and 64 in silicon nitride [34]. To the best of our knowledge, a comparison of p_z in two different materials has not been performed in a single study.

In this letter we study individual TLSs in both polycrystalline alumina $\gamma - \text{Al}_2\text{O}_3$ and amorphous alumina $\alpha - \text{AlO}_x$. We follow the circuit schematic of Ref. [34], and we now name it an Electrical-Bridge Quantum-Defect Sensor (EBQuDS). The TLSs were analyzed in films with an approximate thickness of 20 nm. The TLSs in $\gamma - \text{Al}_2\text{O}_3$ films are relatively stable, and allow us to obtain a large distribution of 394 TLS dipole moments p_z . In $\alpha - \text{AlO}_x$ films, 189 TLS moments are extracted despite higher TLS noise. Compared to the $\gamma - \text{Al}_2\text{O}_3$ film, larger averaged dipole and standard deviation σ are extracted in $\alpha - \text{AlO}_x$ films and 10% of TLSs have larger dipole than the maximum extracted in $\gamma - \text{Al}_2\text{O}_3$. Specific TLS structures were proposed using available information from recent work on density functional theory (DFT) analysis of TLSs in alumina, where both hydrogen [47, 48] and oxygen [49–51] based TLS have been proposed as the interstitial defects. A comparison of the dipole moments for both $\gamma - \text{Al}_2\text{O}_3$ and $\alpha - \text{AlO}_x$ film types allows possible TLS origin identification.

METHOD

Fabrication starts by *in situ* growth of Al/alumina/Al trilayers on a 3-inch Si substrate, where the alumina is the material hosting the TLSs. The *in situ* method prevents substantial hydrogen contamination, but diffusion of hydrogen is also difficult to prevent in standard lithographic processing [52]. Then, a first BCl_3 etch forms a mesa into the top 2 layers, defining 4 equal capacitors ($C_1 - C_4$). Next, a second BCl_3 etch forms the base-metal including a resonator inductor L and ground plane. Finally, silicon nitride is deposited as a wiring dielectric, vias are etched by SF_6 , and an Al wiring layer is defined to connect the inductor to the capacitors. This creates the final resonator structure as shown in Fig. 1 (a). Alumina in the dielectric layer is designed to have an approximate thickness $d = 20$ nm and a volume $V = 1.11 \times 10^{-17} \text{ m}^3$ in each capacitor.

The two sample types are grown in separate chambers. The polycrystalline sample has 20 nm thick $\gamma - \text{Al}_2\text{O}_3$ film deposited by electron-beam evaporation from 99.99% purity Al_2O_3 pellets with a base pressure of $< 5 \times 10^{-7}$ torr and alumina is sandwiched by two 100 nm thick aluminum films. On the other hand, the $\alpha - \text{AlO}_x$ film is 14.7 nm thick with $x = 1.3 \pm 0.1$ and is grown by iterating eight rounds of 1 nm Al deposition followed by static oxidation at 9.5 mbar of oxygen at 250 ° C as de-

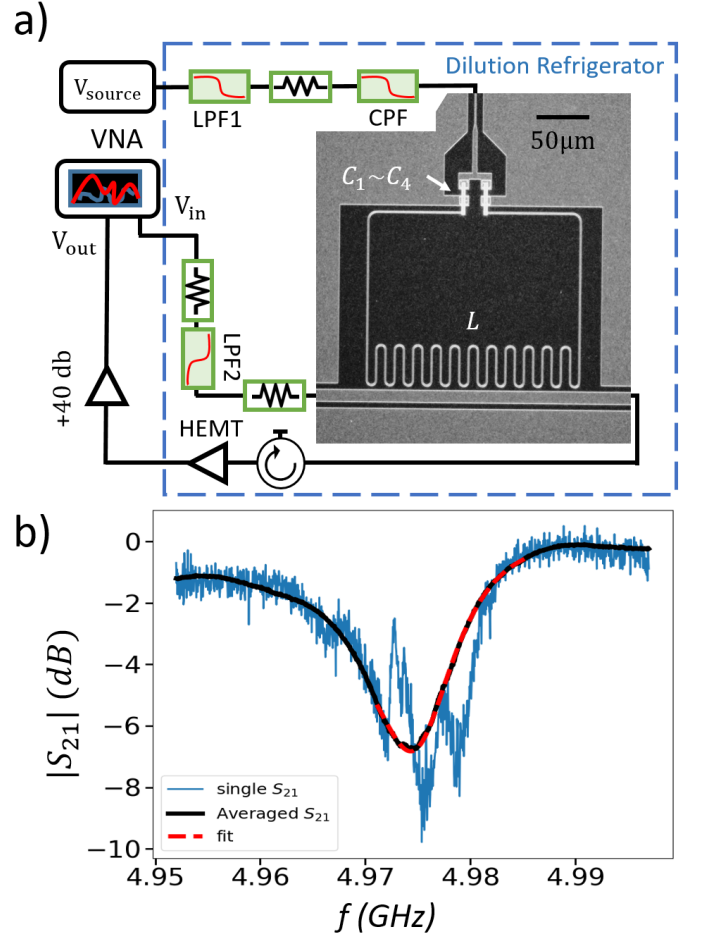


FIG. 1. (a) Optical image of microwave resonator with an abbreviated wiring schematic. The source voltage is filtered through an RC low pass filter and a copper powder filter (CPF). The combination of resistance in the RC filter and the 3dB attenuator gives $V_{\text{bias}} = 9.56 \times 10^{-3} \times V_{\text{source}}$. (b) $|S_{21}|$ of one $\gamma - \text{Al}_2\text{O}_3$ resonator. It shows multiple dips indicating TLSs strongly coupled to the resonator. The black curve is the ensemble average $|S_{21, \text{avg}}|$, obtained by averaging S_{21} from different bias voltages. The intrinsic quality Q_i is $1 / (1.47 \times 10^{-3}) \approx 680$ according to the red fitting line.

scribed in ref. [53]. Given this oxidation condition, no long-range ordered (crystalline) structure was detected from transmission electron microscopy and only 3% unoxidized aluminum was found inside the $\alpha - \text{AlO}_x$ layer. Transmission electron microscopy shows that the thickness can vary from 10 to 20 nm in some rare cases.

The resonator inductively couples to the transmission line so that a 2-port microwave transmission measurement can be carried out. The applied voltage from room temperature is filtered by an RC filter, 3dB attenuator and a copper powder filter. It generates an dc biased field E_{ex} across each capacitor. The maximum E_{ex} is 90 kV/m with which we observe no refrigerator heating, thus no significant leakage current. Two resonators were fabricated per chip with nominally the same capacitors,

but with different value inductors, giving resonance frequencies of approximately $f_0 = 5.0$ GHz and 4.4 GHz. The resonators were measured at or below 60 mK. A less than 1 probing photon number \bar{n} is used for all the reported data, to allow observation of TLSs near their ground state.

With a known external field E_{ex} , the asymmetry energy Δ is shifted as $\Delta' = \Delta + 2p_z E_{\text{ex}}$ [34]. Therefore, the resultant TLS energy is

$$E = \sqrt{(\Delta + 2p_z E_{\text{ex}})^2 + \Delta_0^2} \quad (2)$$

The resonator constitutes a circuit QED system with a Jaynes-Cummings model modified for many TLSs. TLSs can be resolved individually by the resonator when the cooperativity $g^2/\gamma_{\text{TLS}}\kappa \geq 1$ [54], where γ_{TLS} is the TLS decay rate for the strongly coupled TLS, and $\kappa = \kappa_e + \kappa_i$ is the resonator decay rate from external coupling and internal loss. We increase the g and cooperativity by reducing V , since $E_{rms} = \sqrt{\hbar f_0/8\epsilon_r\epsilon_0 V}$ in our parallel-plate capacitor resonator [8].

A single transmission trace $|S_{21}|$ is shown in Fig. 1 (b) from a $\gamma - \text{Al}_2\text{O}_3$ resonator. Within the bandwidth of the resonator, a few fine resonance dips reveal the energies of individual TLSs. However, the TLSs often only couple weakly to the resonator. Therefore, we obtain an approximate intrinsic material loss tangent $\tan \delta_0$ by using the averaged S_{21} traces from different voltage biases, yielding an ensemble-averaged $S_{21,avg}$. The $|S_{21,avg}|$ component of the result is shown as the solid black curve in Fig. 1 (b). A fit (dashed red curve) to $S_{21,avg}$ yields $\tan \delta_0 = 1/Q_i = 1/680 = 1.5 \times 10^{-3}$ and the external (or coupling) quality factor is extracted as $Q_e = 2\pi f_0/\kappa_e = 590$. The same procedure performed on a $-\text{AlO}_x$ gives an intrinsic loss tangent of $\tan \delta_0 = 1/\bar{Q}_i = 1/1020 = 9.8 \times 10^{-4}$, which is smaller than that of $\gamma - \text{Al}_2\text{O}_3$. \bar{Q}_i is the averaged Q_i of a $-\text{AlO}_x$ and its Q_i are distinct with every cooldown unlike $\gamma - \text{Al}_2\text{O}_3$ [55]. Our loss tangents are similar to alumina with different growth methods, where the loss is measured at $\tan \delta_0 = 1.6 \times 10^{-3}$ [8, 56], 7×10^{-4} [57], and 1.6×10^{-3} [58]. Below we discuss TLSs measured in both alumina film types using two resonators for each type.

RESULTS AND DISCUSSION

Fig. 2 (a) shows a TLS spectrum example, $|S_{21}|$, as a function of frequency f and the dc-field E_{ex} for $\gamma - \text{Al}_2\text{O}_3$ measured on one of the two resonators during one cooldown. TLS energies exhibit hyperbolic energies versus E_{ex} , as shown in Fig. 2 (a) in agreement with Eq. 2. Similar spectra have been observed and analyzed in a previous study on silicon nitride [34]. One can estimate the Δ_0 from the minimum of the TLS energy ($\hbar f_m = \Delta_0$),

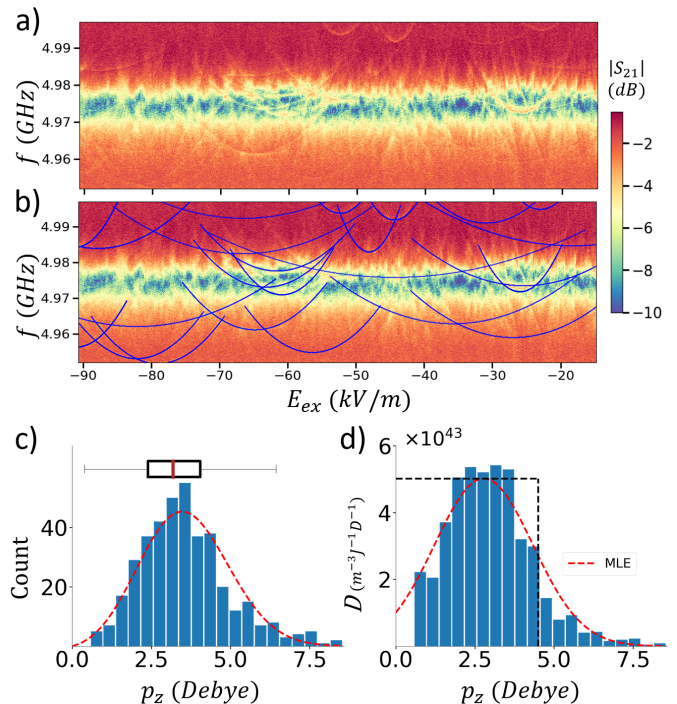


FIG. 2. Data on nanoscale thick $\gamma - \text{Al}_2\text{O}_3$ (polycrystalline) film in cQED system (a) Color scale plot of transmission $|S_{21}|$ vs. frequency f and electric field E_{ex} . Data show a main resonance at 4.974 GHz. Several local minima in $|S_{21}|$ reveal the energy of individual TLSs. (b) Several TLSs in blue hyperbolas are fitted to the energy model (Eq. 2), where p_z comes from the curvature of the energy hyperbola. (c) The entire data set from this film type yields 394 moments p_z . The red dashed line is a Gaussian function multiplied by p_z as fit to data. A Seaborn box is plotted, where the red color line is the mean line and the right and left side of box represent 25th and 75th percentage of dipole data. (d) Material TLS density of p_z after accounting for the experimental weighing factor. A red dashed Gaussian line is shown with the corresponding fit parameters in (c). From the fit we report the material mean p_z of 2.6 D and standard deviation $\sigma = 1.6$ D. The black dashed line illustrates a possible material density if we assume an isotropic TLS direction.

and p_z from the hyperbola – a steeper curvature gives a larger dipole moment. A optimized Monte Carlo fit is performed on each TLS energy to extract p_z of the specific TLS (see supplementary for detailed fitting procedure [55]). Only well defined TLS energy curves are selected for analysis. Example fits are plotted as blue hyperbolas in Fig. 2 (b).

TLSs change their energies randomly during cool-downs from room temperature. From four different cool-downs, we created different sets of TLSs in the two resonators with one material type. According to the standard TLS distribution [41], TLSs have log-uniform tunneling energies such that there are negligible distribution changes for TLS tunneling energies that are only 0.6 GHz

different in our two resonator frequencies (see supplementary for each data [55]). We therefore combine all the data from different runs in the two resonators to enlarge the sampling number and improve the statistics: a total of 394 TLSs from two resonators are analyzed to form the measured p_z distribution $H(p_z)$ with an average of 3.5 ± 0.4 Debye (D) shown in Fig. 2 (c). The accuracy of extraction is limited by the uniformity of thickness of alumina rather than fitting process. A large amounts of individual TLSs allow relatively accurate representation of the TLS moments in $\gamma - \text{Al}_2\text{O}_3$.

Though the measured polycrystalline distribution $H(p_z)$ has a mean value of 3.5 D, this is not an intrinsic material property. At a given electric field bias range ΔE_{ex} , TLSs with larger dipole moments have a larger shift in asymmetry energy Δ' relative to smaller moments, and this leads to a higher probability of the former moments having their energy minimum within the resonator bandwidth (see supplementary for derivation [55] and Ref [34]). The intrinsic material TLS dipole distribution $D(p_z)$ is related to TLS material density $P_0 = \int D(p_z) dp_z$ (in units of $J^{-1}m^{-3}$), and can be calculated from $D(p_z) = \frac{1}{V} \frac{H(p_z)}{2p_z} \frac{1}{\Delta E_{ex}} \frac{f_0}{\Delta f_0}$ [55], where f_0 is the resonator frequency and Δf_0 is the frequency span of the S_{21} measurement. The red dashed line in Fig. 2 (c) shows a fit using a maximum likelihood estimation (MLE) method. The fitting function is a modified Gaussian distribution multiplied by p_z [55]. The TLS material density $D(p_z)$ is shown in Fig. 2 (d), where the red line shows a Gaussian function matching the fit parameters in Fig. 2 (c).

From the fit, we find that the polycrystalline material distribution $D(p_z)$ has a fit mean dipole moment of $\bar{p}_z = 2.6 \pm 0.3$ D ($= 0.54 \pm 0.05$ eÅ) and $\sigma = 1.6$ D ($= 0.33$ eÅ). The computed TLS density P_0 is $1.0 \pm 0.1 \times 10^{44} (J^{-1}m^{-3})$. This computed value of TLS density along with the dipole moments agrees with the measured loss tangent. As a result we used the material units in panel (d) for the distribution $D(p_z)$.

For amorphous samples or random voids within polycrystals, we expect TLS dipoles to be random in angle (isotropic). For a case of one single dipole magnitude p_0 and uniform distribution in $\cos\theta$, where θ is the angle of dipole to z-axis, results isotropy. Therefore, $D(p_z)$ is expected to be independent of p_z until the maximum value p_0 . As a guide to the eye, an isotropic distribution (random angle) with dipole moment $p_0 = 4.5$ D is shown as a black dashed line in Fig. 2 (d). The positive slope in the observed distribution indicates that we have a departure from isotropic distribution (isotropic TLSs give only non-positive slope). Thus, data in Fig. 2 (d), shows that $\gamma - \text{Al}_2\text{O}_3$ TLSs can be different than the standard model for TLSs (designated for amorphous samples [41, 42]). The anisotropic angular distribution may be caused by the polycrystalline film texture (crystallite orientation)

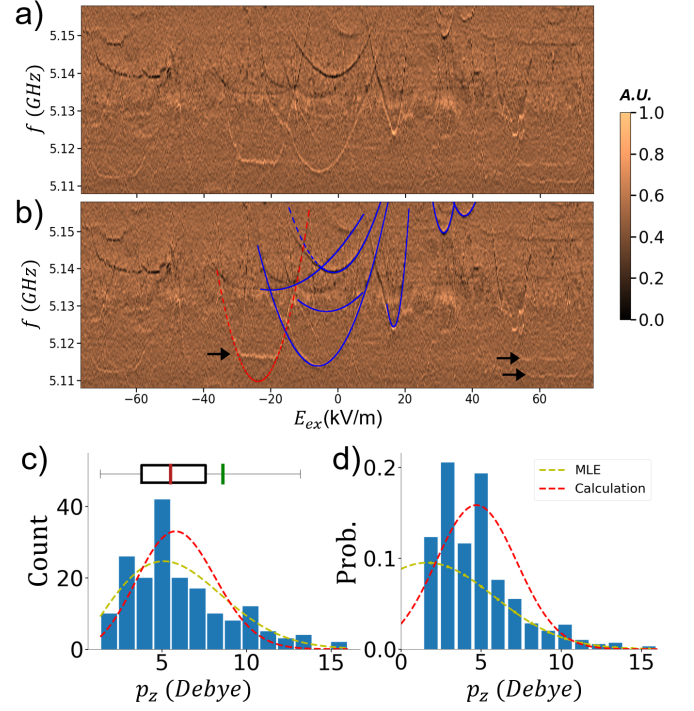


FIG. 3. (a) Example of processed transmission data on amorphous $a - \text{AlO}_x$ film resonator versus frequency f and external electric field E_{ex} (see main text). The LC resonance is approximately 5.132 GHz (no longer visible after data processing). (b) The same data with traces fit to TLS energy function. 7 fitted dipole moments are extracted at values of 3.2 - 12.7 D. TLSs whose energy does not depend on bias voltage are marked by arrows. Curved red dashed trace shows an anomalous TLS; it switches between a hyperbola and a nearly constant energy of 5.116 GHz at $E_{ex} = -30$ kV/m and $E_{ex} = -18$ kV/m. (c) The measured distribution of 189 TLSs and a Seaborn box. The green line represents the largest dipole measured in $\gamma - \text{Al}_2\text{O}_3$. (d) The probability of the material TLS dipole distribution. Dashed lines in (c) and (d) are modified and regular Gaussian functions and obtained by two methods. The red lines are acquired by calculation, and the yellow lines are acquired by fitting. We report a mean dipole $= 4.6 \pm 0.5$ D and $\sigma = 2.5 \pm 0.3$ D. Analysis on missing extracted dipoles was needed in the amorphous film, but it also gives a mean value much larger than in the $\gamma - \text{Al}_2\text{O}_3$ (see main text and supplementary).

which influences the TLS orientation.

Fig. 3 (a) shows transmission spectroscopy results for $a - \text{AlO}_x$. However, the $a - \text{AlO}_x$ spectra are not as clear as in $\gamma - \text{Al}_2\text{O}_3$ due to higher noise in the spectra, despite using the same setup. To improve the TLS signal contrast, the transmission (S_{21}) data is shown after processing, unlike the polycrystalline film data shown earlier. For our first processing step we chose to subtract $S_{21,avg}$ from S_{21} , and increase further contrast using the formula $(S_{21}(dB) - S_{21,avg}(dB)) \times |S_{21,avg}|$. As a second and third processing step, we apply a low-pass filter in the frequency direction and then take the derivative

with respect to frequency. The final result is plotted in arbitrary unit (AU) in Fig. 3 (a) and (b) and we added hyperbolic fitting traces (blue lines) to the panel (b).

As we will show in detail below, TLSs within a γ - Al_2O_3 are less stable than those in α - AlO_x – the former TLSs show sudden switchings in energy or even become invisible in time within the resonator bandwidth, making it more difficult to identify individual TLSs. This leads to a higher error in the Monte Carlo fit. We also observed energy features that are almost independent of E_{ex} , as indicated by black arrows. They are not expected because all coupled TLSs should be frequency tunable in the device. At -8 kV/m, one hyperbola seems to change slope (as indicated by the start of a blue dashed line), although instead this event may represent a transition in observing two separate TLSs.

Surprisingly, one of them seems to be only partially described by hyperbola in red-dashed curve. Increasing bias voltage at -30 kV/m, this TLS seems to switch from a regular TLS state to an unknown state which has constant transition energy under bias until -19 kV/m, and finally switch back to normal TLS behavior. This indicates an unexpected state near its energy minima Δ_0 , which we believe has not been identified previously.

Unlike the other sample, the amorphous films show most of the hyperbolas from TLSs in the bias range of -30 to 30 kV/m (more data in [55]). Outside of this range TLSs tracks are seen, but they don't trace out a smooth hyperbola. Furthermore, we find that the most TLSs do not appear twice after repeating the voltage scanning within the same cool-down. In a small fraction of TLS hyperbola (< 3%) a TLS hyperbola has the same dipole and the minimum in energy is within 1 MHz, such that it is regarded as the same TLS and disregarded in distribution.

In α - Al_2O_3 , we identify and analyze a total of 189 TLSs using multiple field sweeps and cool-downs according to the above procedure. The measured distribution $H(p_z)$ with counts and the probability of material distribution $D(p_z)$ are shown in Fig. 3 (c). The extracted p_z shows a broad range in value from 0.5 to 16 D with an average of 6.0 D and the interquartile range (range from the 25th to 75th points) of 3.8 D. Because of the large deviation, we cannot get a reasonable fitting to a Gaussian from the MLE method as shown in yellow lines, which have mean value of 1.6 D and standard deviation of 4.2 D. Instead, we calculate the material average dipole moment \bar{p}_z for $D(p_z)$ from $H(p_z)$, using $\bar{p}_z = \int p_z D(p_z) dp_z / \int D(p_z) dp_z = \int H(p_z) dp_z / \int p_z^{-1} H(p_z) dp_z$, and the standard deviation in a similar way. From this we find $\bar{p}_z = 4.6 \pm 0.5$ ($= 0.96 \pm 0.1$ eÅ) and $\sigma = 2.5 \pm 0.3$ D ($= 0.52 \pm 0.05$ eÅ). A Gaussian curve with these parameters are plotted as red dashed line.

The calculated loss from the dipole distribution is 3.2×10^{-4} which is smaller than 9.75×10^{-4} reported

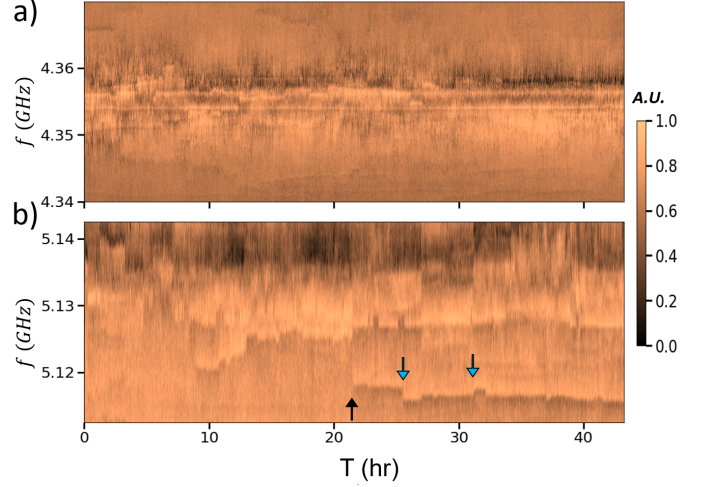


FIG. 4. Time dependence of processed $|S_{21}|$ with a frequency range ≥ 30 MHz. (a) γ - Al_2O_3 spectroscopy versus time shows the TLSs are relatively stable in frequency near the transmission minimum for 10s of hours. (b) α - AlO_x spectroscopy versus time shows relatively large TLS energy switching and drift.

above. The missing TLS extraction happens in two ways. On one hand, larger p_z TLSs have a higher possibility to interact with other TLSs and their frequencies are prone to switch to other states or diffuse. On the other hand, small p_z TLSs require longer time to acquire TLS hyperbolas and the signal-to-noise ratio is smaller due to smaller coupling to the resonator. As a result, the TLS extraction does not include most of the TLS unlike the extraction in γ - Al_2O_3 . We estimate the minimum mean moment of amorphous alumina from missing TLSs. We make no claim about anisotropy in this film since the missing TLSs may create one of the peaks in the distribution of p_z [55].

To decipher the role of TLS-TLS interaction, we next conduct temporal spectroscopes for the two different film types: γ - Al_2O_3 and α - AlO_x . Fig. 4 shows processed S_{21} traces observed over many hours. This resonant TLS noise is believed to be caused by interactions with thermally excited low-frequency TLSs [13, 59]. As shown in Fig. 4 (a), TLSs biased at 0 V in γ - Al_2O_3 films near the resonance frequency are relatively stable – their energies drift by less than 2 MHz over tens of hours. On the contrary, TLSs in α - AlO_x behave similar to Ref. [13]. TLSs show irregular drifts of more than 5 MHz, including multiple telegraphic switching events (blue arrows) and abrupt TLS shifts (black arrow). Due to the larger dipole moments observed in α - AlO_x , we expect a larger interaction than that in γ - Al_2O_3 (assuming that the low-frequency thermally activated TLSs are similar to the high frequency ones). The large unstable behaviors shown in the amorphous films occur in a few hours, e.g., a 4 D hyperbola track in α - AlO_x data took about

5 hours to obtain.

Comparable results on amorphous alumina exist. One study found p_z in the range of 2.3 - 7.4 D, using a few analyzed TLSs [40]. Other field tuned measurements in a-AlOx, studying the barrier of JJs, detected several moments with $p_z = 1.0 - 2.9$ D [35]. Measurements of the transition dipole moments in a-AlOx of JJs indicate that $p_z \leq 6.0$ D [8] and $p_z \leq 4.8$ D [60] in two TLS dipoles measured. The existing data on amorphous alumina TLSs seems consistent with our observations, though the growth methods are slightly different.

Finally, we return to comment on the possible origins of TLSs in our alumina from a comparison to recent TLS DFT [47–50] and molecular dynamics [51] simulations on aluminum oxide. Two models related to hydrogen(H) suggest total dipole moment $p < 3.0$ D [47, 48]. Holder *et al.* find that hydrogen aluminum-vacancy TLSs $V_{Al} - H$ in $\alpha - Al_2O_3$ have $p = 3.0$ D [47]. Separately, Gordon *et al.* simulated the interstitial hydrogen in $\alpha - Al_2O_3$ at various two oxygen(O) atoms distances where $p = 2.2 - 2.7$ D [48]. Besides H-based simulations, two models of O-based TLSs suggest $p > 4.2$ D. DuBois *et al.* studied models of delocalized oxygen atoms with six neighboring aluminum atoms [49, 50]. They found oxygen deficient AlO_x for $x = 1.25$ by varying distances between O and Al atoms, with $p = 4.2 - 6.5$ D for TLSs with tunneling energy $\Delta_0/h = 4$ GHz [49]. Additionally, Paz *et al.* find natural bi-stable structures in amorphous alumina including only Al and O atoms and calculate an average $p = 4.2$ D from 7 TLSs [51]. Although there are difference between theoretical models, they are consistent in that H-TLSs have smaller p than O-TLSs.

The $\gamma - Al_2O_3$ $D(p_z)$ has a single peak at approximately $p_z = 2.6$ D, which can be sourced from H-TLS or two unresolved peaks of both H- and O-TLSs. Although small in statistics, a - AlO_x has a wider spread in $D(p_z)$ and two separate peaks. Furthermore, a - AlO_x TLSs have 10 % population with $p_z > 8.6$ D, where $p_z = 8.6$ D is the maximum in $\gamma - Al_2O_3$. Using a comparison between two alumina datasets and the fact that O-based TLS is the larger dipole in DFT structures, we find a higher ratio of O-TLSs to H-TLSs in a-AlOx than $\gamma - Al_2O_3$.

CONCLUSION

In summary, we have extracted the dipole moment p_z of hundreds of individual TLSs in nanoscale-thick films of (polycrystalline) $\gamma - Al_2O_3$ and (amorphous) a - AlO_x alumina. We have used an Electrical-Bridge Quantum Defect Sensor (EBQuDS), which we show is suitable to characterize number of TLSs as quantum defects. Analysis of the measured histogram of p_z reveals that polycrystalline alumina fits well to a single Gaussian peak. From the material distribution (algebraically related to

the measured one), we obtain that the mean TLS moment of the polycrystalline film is $p_z = 2.6 \pm 0.3$ D ($= 0.54 \pm 0.05$ eÅ) and $\sigma = 1.6 \pm 0.2$ D ($= 0.33 \pm 0.03$ eÅ). Furthermore, the material distribution disagrees with the isotropic model commonly used in amorphous materials, indicative of a preferred texture (orientation) of the polycrystalline grains which host TLSs. On the other hand, we cannot conclude if amorphous alumina dipoles are isotropic or not because of missing TLSs extraction.

The ability to extract an accurate mean p_z puts constraints on its defect type, and allows us to make first comparisons to new microscopic structures used in DFT calculations. The polycrystalline data show one dominant peak, and could be showing dominance of H-TLSs, or unresolved peaks of both H- and O-TLSs in the distribution. We find that a - AlO_x has a larger mean $p_z = 4.6 \pm 0.5$ D, which is consistent with previous amorphous alumina results. In contrast to $\gamma - Al_2O_3$, the TLSs switch more rapidly, and our p_z distribution in amorphous alumina yields a larger standard deviation ($= 2.5 \pm 0.3$ D) and two peaks in contrast to one. The moments above 8.6 D (10% of the distribution) are larger than any TLS in polycrystalline alumina and agree only with calculations of delocalized O atoms. Due to this and other amorphous distribution features, we find that the ratio of O- to H-TLSs is higher in amorphous samples than in the polycrystalline ones. Because of its relative simplicity in distribution, alumina seems to be an important material for further JJ-barrier studies.

ACKNOWLEDGEMENTS

We acknowledge Lukas Radke, Hannes Rotzinger (both from Physikalisches Institut, Karlsruhe Institute of Technology, Germany) and Martin Weides (James Watt School of Engineering, University of Glasgow, UK) for support of discussions on amorphous alumina sample growth.

-
- [1] Y. Nakamura, Y. A. Pashkin, and J. S. Tsai, *nature* **398**, 786 (1999).
 - [2] A. Wallraff, D. I. Schuster, A. Blais, L. Frunzio, R.-S. Huang, J. Majer, S. Kumar, S. M. Girvin, and R. J. Schoelkopf, *Nature* **431**, 162 (2004).
 - [3] V. E. Manucharyan, J. Koch, L. I. Glazman, and M. H. Devoret, *Science* **326**, 113 (2009).
 - [4] M. H. Devoret and R. J. Schoelkopf, *Science* **339**, 1169 (2013).
 - [5] F. Yan, S. Gustavsson, A. Kamal, J. Birenbaum, A. P. Sears, D. Hover, T. J. Gudmundsen, D. Rosenberg, G. Samach, S. Weber, *et al.*, *Nature communications* **7**, 1 (2016).

- [6] F. Arute, K. Arya, R. Babbush, D. Bacon, J. C. Bardin, R. Barends, R. Biswas, S. Boixo, F. G. Brandao, D. A. Buell, *et al.*, *Nature* **574**, 505 (2019).
- [7] R. W. Simmonds, K. Lang, D. A. Hite, S. Nam, D. P. Pappas, and J. M. Martinis, *Physical Review Letters* **93**, 077003 (2004).
- [8] J. M. Martinis, K. B. Cooper, R. McDermott, M. Steffen, M. Ansmann, K. Osborn, K. Cicak, S. Oh, D. P. Pappas, R. W. Simmonds, *et al.*, *Physical review letters* **95**, 210503 (2005).
- [9] J. Burnett, L. Faoro, I. Wisby, V. Gurtovoi, A. Chernykh, G. Mikhailov, V. Tulin, R. Shaikhaidarov, V. Antonov, P. Meeson, *et al.*, *Nature communications* **5**, 1 (2014).
- [10] S. M. Meißner, A. Seiler, J. Lisenfeld, A. V. Ustinov, and G. Weiss, *Physical Review B* **97**, 180505 (2018).
- [11] J. J. Burnett, A. Bengtsson, M. Scigliuzzo, D. Niepce, M. Kudra, P. Delsing, and J. Bylander, *npj Quantum Information* **5**, 1 (2019).
- [12] C. Müller, J. Lisenfeld, A. Shnirman, and S. Poletto, *Physical Review B* **92**, 035442 (2015).
- [13] P. Klimov, J. Kelly, Z. Chen, M. Neeley, A. Megrant, B. Burkett, R. Barends, K. Arya, B. Chiaro, Y. Chen, *et al.*, *Physical review letters* **121**, 090502 (2018).
- [14] S. Schlör, J. Lisenfeld, C. Müller, A. Bilmes, A. Schneider, D. P. Pappas, A. V. Ustinov, and M. Weides, *Physical review letters* **123**, 190502 (2019).
- [15] E. J. Connors, J. Nelson, H. Qiao, L. F. Edge, and J. M. Nichol, *Physical Review B* **100**, 165305 (2019).
- [16] O. Noroozian, J. Gao, J. Zmuidzinas, H. G. LeDuc, and B. A. Mazin, in *AIP Conference Proceedings*, Vol. 1185 (American Institute of Physics, 2009) pp. 148–151.
- [17] J. Gao, *The physics of superconducting microwave resonators*, Ph.D. thesis, California Institute of Technology (2008).
- [18] A. D. O’Connell, M. Ansmann, R. C. Bialczak, M. Hofheinz, N. Katz, E. Lucero, C. McKenney, M. Neeley, H. Wang, E. M. Weig, *et al.*, *Applied Physics Letters* **92**, 112903 (2008).
- [19] E. H. Lock, P. Xu, T. Kohler, L. Camacho, J. Prestigiacomo, Y. J. Rosen, and K. D. Osborn, *IEEE Transactions on Applied Superconductivity* **29**, 1 (2019).
- [20] J. B. Chang, M. R. Vissers, A. D. Córcoles, M. Sandberg, J. Gao, D. W. Abraham, J. M. Chow, J. M. Gambetta, M. Beth Rothwell, G. A. Keefe, *et al.*, *Applied Physics Letters* **103**, 012602 (2013).
- [21] J. Goetz, F. Deppe, M. Haeberlein, F. Wulschner, C. W. Zollitsch, S. Meier, M. Fischer, P. Eder, E. Xie, K. G. Fedorov, *et al.*, *Journal of Applied Physics* **119**, 015304 (2016).
- [22] C. Quintana, A. Megrant, Z. Chen, A. Dunsworth, B. Chiaro, R. Barends, B. Campbell, Y. Chen, I.-C. Hoi, E. Jeffrey, *et al.*, *Applied Physics Letters* **105**, 062601 (2014).
- [23] L. Grünhaupt, U. von Lüpke, D. Gusenkova, S. T. Skacel, N. Maleeva, S. Schlör, A. Bilmes, H. Rotzinger, A. V. Ustinov, M. Weides, *et al.*, *Applied Physics Letters* **111**, 072601 (2017).
- [24] H. Paik, D. Schuster, L. S. Bishop, G. Kirchmair, G. Catelani, A. Sears, B. Johnson, M. Reagor, L. Frunzio, L. Glazman, *et al.*, *Physical Review Letters* **107**, 240501 (2011).
- [25] C. Wang, C. Axline, Y. Y. Gao, T. Brecht, Y. Chu, L. Frunzio, M. Devoret, and R. J. Schoelkopf, *Applied Physics Letters* **107**, 162601 (2015).
- [26] O. Dial, D. T. McClure, S. Poletto, G. Keefe, M. B. Rothwell, J. M. Gambetta, D. W. Abraham, J. M. Chow, and M. Steffen, *Superconductor Science and Technology* **29**, 044001 (2016).
- [27] C. Deng, (2015).
- [28] D. L. Creedon, Y. Reshitnyk, W. Farr, J. M. Martinis, T. L. Duty, and M. E. Tobar, *Applied Physics Letters* **98**, 222903 (2011).
- [29] K.-H. Lee, S. Chakram, S. E. Kim, F. Mujid, A. Ray, H. Gao, C. Park, Y. Zhong, D. A. Muller, D. I. Schuster, *et al.*, *Nano letters* **19**, 8287 (2019).
- [30] J. I.-J. Wang, D. Rodan-Legrain, L. Bretheau, D. L. Campbell, B. Kannan, D. Kim, M. Kjaergaard, P. Krantz, G. O. Samach, F. Yan, *et al.*, *arXiv preprint arXiv:1809.05215* (2018).
- [31] Y.-P. Shim and C. Tahan, *Nature communications* **5**, 1 (2014).
- [32] S. Oh, K. Cicak, J. S. Kline, M. A. Sillanpää, K. D. Osborn, J. D. Whittaker, R. W. Simmonds, and D. P. Pappas, *Physical Review B* **74**, 100502 (2006).
- [33] M. P. Weides, J. S. Kline, M. R. Vissers, M. O. Sandberg, D. S. Wisbey, B. R. Johnson, T. A. Ohki, and D. P. Pappas, *Applied Physics Letters* **99**, 262502 (2011).
- [34] B. Sarabi, A. N. Ramanayaka, A. L. Burin, F. C. Wellstood, and K. D. Osborn, *Physical review letters* **116**, 167002 (2016).
- [35] A. Bilmes, S. Volosheniuk, J. D. Brehm, A. V. Ustinov, and J. Lisenfeld, *npj Quantum Information* **7**, 1 (2021).
- [36] A. Bilmes, A. Megrant, P. Klimov, G. Weiss, J. M. Martinis, A. V. Ustinov, and J. Lisenfeld, *Scientific reports* **10**, 1 (2020).
- [37] S. de Graaf, S. Mahashabde, S. Kubatkin, A. Y. Tzalenchuk, and A. Danilov, *Physical Review B* **103**, 174103 (2021).
- [38] J. Lisenfeld, C. Müller, J. H. Cole, P. Bushev, A. Lukashenko, A. Shnirman, and A. V. Ustinov, *Physical review letters* **105**, 230504 (2010).
- [39] G. J. Grabovskij, T. Peichl, J. Lisenfeld, G. Weiss, and A. V. Ustinov, *Science* **338**, 232 (2012).
- [40] J. D. Brehm, A. Bilmes, G. Weiss, A. V. Ustinov, and J. Lisenfeld, *Applied Physics Letters* **111**, 112601 (2017).
- [41] P. W. Anderson, B. Halperin, and C. M. Varma, *Philosophical Magazine* **25**, 1 (1972).
- [42] W. Phillips, *Journal of Low Temperature Physics* **7**, 351 (1972).
- [43] S. de Graaf, L. Faoro, L. Ioffe, S. Mahashabde, J. Burnett, T. Lindström, S. Kubatkin, A. Danilov, and A. Y. Tzalenchuk, *Science Advances* **6**, eabc5055 (2020).
- [44] C. C. Yu and H. M. Carruzzo, *arXiv preprint arXiv:2101.02787* (2021).
- [45] M. Khalil, S. Gladchenko, M. Stoutimore, F. Wellstood, A. Burin, and K. Osborn, *Physical Review B* **90**, 100201 (2014).
- [46] S. Matityahu, H. Schmidt, A. Bilmes, A. Shnirman, G. Weiss, A. V. Ustinov, M. Schechter, and J. Lisenfeld, *npj Quantum Information* **5**, 1 (2019).
- [47] A. M. Holder, K. D. Osborn, C. Lobb, and C. B. Musgrave, *Physical review letters* **111**, 065901 (2013).
- [48] L. Gordon, H. Abu-Farsakh, A. Janotti, and C. G. Van de Walle, *Scientific reports* **4**, 1 (2014).
- [49] T. C. DuBois, M. C. Per, S. P. Russo, and J. H. Cole, *Physical review letters* **110**, 077002 (2013).
- [50] T. C. DuBois, S. P. Russo, and J. H. Cole, *New Journal of Physics* **17**, 023017 (2015).

- [51] A. P. Paz, I. V. Lebedeva, I. V. Tokatly, and A. Rubio, *Physical Review B* **90**, 224202 (2014).
- [52] C. G. Van de Walle and J. Neugebauer, *Nature* **423**, 626 (2003).
- [53] S. Fritz, L. Radtke, R. Schneider, M. Luysberg, M. Weides, and D. Gerthsen, *Physical Review Materials* **3**, 114805 (2019).
- [54] B. Sarabi, A. N. Ramanayaka, A. L. Burin, F. C. Wellstood, and K. D. Osborn, *Applied Physics Letters* **106**, 172601 (2015).
- [55] .
- [56] M. Stoutimore, M. Khalil, C. Lobb, and K. Osborn, *Applied Physics Letters* **101**, 062602 (2012).
- [57] M. Khalil, M. Stoutimore, S. Gladchenko, A. Holder, C. Musgrave, A. Kozen, G. Rubloff, Y. Liu, R. Gordon, J. Yum, *et al.*, *Applied Physics Letters* **103**, 162601 (2013).
- [58] D. P. Pappas, M. R. Vissers, D. S. Wisbey, J. S. Kline, and J. Gao, *IEEE Transactions on Applied Superconductivity* **21**, 871 (2011).
- [59] L. Faoro and L. B. Ioffe, *Physical review letters* **109**, 157005 (2012).
- [60] Y. Shalibo, Y. Rofer, D. Shwa, F. Zeides, M. Neeley, J. M. Martinis, and N. Katz, *Phys. Rev. Lett.* **105**, 177001 (2010).